Nature Communications

https://doi.org/10.1038/s41467-026-69051-6

Article in Press

Chlorination-controlled aggregation and film-formation kinetics enabling high-efficiency organic solar cells with low-cost linear conjugated polymers

Received: 22 July 2025

Accepted: 25 January 2026

Cite this article as: Yin, B., Chen, Z., Wu, B. *et al.* Chlorination-controlled aggregation and film-formation kinetics enabling high-efficiency organic solar cells with low-cost linear conjugated polymers. *Nat Commun* (2026). https://doi.org/10.1038/s41467-026-69051-6

Bingyan Yin, Zhili Chen, Baoqi Wu, Xiyue Yuan, Cong Xiao, Xia Zhou, Jianbin Zhong, Seunglok Lee, Wei Chen, Lifu Zhang, Liming Wang, Guangye Zhang, Wei Zhang, Changduk Yang, Zhitian Liu, Fei Huang, Yong Cao & Chunhui Duan

Chlorination-Controlled Aggregation and Film-Formation Kinetics Enabling High-Efficiency Organic Solar Cells with Low-Cost Linear Conjugated Polymers

Bingyan Yin[1,2,†], Zhili Chen[1,2,3,†], Baoqi Wu[1,2]*, Xiyue Yuan[1,2], Cong Xiao[1,2], Xia Zhou[4], Jianbin Zhong[5], Seunglok Lee[6], Wei Chen[7], Lifu Zhang[8], Liming Wang[9]*, Guangye Zhang[7], Wei Zhang[5], Changduk Yang[6], Zhitian Liu[3]*, Fei Huang[1,2], Yong Cao[1,2] and Chunhui Duan[1,2]*

[1]Institute of Polymer Optoelectronic Materials and Devices, State Key Laboratory of Luminescent Materials and Devices, South China University of Technology, Guangzhou, P. R. China

[2]Guangdong Basic Research Center of Excellence for Energy & Information Polymer Materials, South China University of Technology, Guangzhou, P. R. China

[3]Institute of Materials for Optoelectronics and New Energy, School of Materials Science and Engineering, Wuhan Institute of Technology, Wuhan, P. R. China

[4]School of New Energy, Ningbo University of Technology, Ningbo, P. R. China

[5]School of Physics and Materials Science, Guangzhou University, Guangzhou, P. R. China

[6]School of Energy and Chemical Engineering, Ulsan National Institute of Science and Technology, Ulsan, South Korea

[7]College of New Materials and New Energies, Shenzhen Technology University, Shenzhen 518118, P. R. China

[8]School of Chemical Engineering, Key Lab of Fluorine and Silicon for Energy Materials and Chemistry of Ministry of Education, Jiangxi Normal University, Nanchang, P. R. China

[9]Spallation Neutron Source Science Center, Dongguan 523803, P.R. China, Institute of High Energy Physics, Chinese Academy of Sciences, Beijing 100049, P.R. China

[†]These authors contributed equally

Corresponding author

Baoqi Wu, E-mail: wubaoqilc@scut.edu.cn

Liming Wang, E-mail: wanglm@ihep.ac.cn

Zhitian Liu, E-mail: able.ztliu@wit.edu.cn
Chunhui Duan, E-mail: duanchunhui@scut.edu.cn

Abstract

The pursuit of simple yet high-performance materials is important for advancing organic photovoltaics, though structurally simple polymer donors typically underperform. This study reveals precise control over polymer aggregation and donor-acceptor compatibility is key to optimizing active layer morphology. We design three linear conjugated polymers with systematically chlorinated backbones to finely modulate aggregation tendency and surface tension. This strategy concurrently regulates film-formation kinetics and donor-acceptor compatibility. PTTz-Cl50 exhibits ideal aggregation and optimal compatibility with BTP-eC9, enabling sequential deposition that forms a bicontinuous interpenetrating network with appropriate domain size and marked phase purity. This microstructure provides sufficient interfacial area for exciton dissociation while retaining high-purity charge transport pathways. Consequently, the device demonstrates rapid exciton dissociation, efficient charge transport, and suppressed recombination, enhancing both short-circuit current and fill factor. This yield a high power conversion efficiency of 20.42% for linear conjugated polymers, underscoring the promise of low-cost materials for efficient devices.

Introduction

Organic solar cells (OSCs) have emerged as a promising candidate for next-generation photovoltaics, owing to their unique attributes such as lightweight, flexibility, and suitability for solution-based large-area fabrication.[1-3] The field has witnessed remarkable progress in power conversion efficiencies (PCEs), now exceeding 20%,[4] primarily driven by innovations in non-fullerene acceptors (NFAs) including the ITIC,[5] IT-4F,[6] Y6,[7] and subsequent derivative families.[8-11] While the NFA library has expanded considerably, the development of high-performance polymer donors has progressed at a slower pace, creating a noticeable imbalance in the material portfolio available for efficient OSC devices. Current high-performance polymer donors, exemplified by PM6,[12] D18,[13] and PBQx-TF[14] (Supplementary Fig. 1), rely predominantly on two-dimensional conjugated (2D-conjugated) thiophene-substituted benzodithiophene (BDTT)-based polymers.[15-18] These polymers typically require extended conjugated backbones and complex molecular

structures to precisely tailor absorption spectra, energy levels, and crystallinity properties. Such structural complexity increases syntheses difficulties and production costs, hindering the industrialization of OSCs. In contrast, linear conjugated polymers lack suspended side-conjugated blocks, featuring simpler structures and more straightforward synthesis routes, which make them more suitable for cost-effective, scalable OSC fabrication.[19-24] However, their photovoltaic performance still lags behind BDTT-based polymers, primarily due to challenges in controlling nanoscale morphology.

Photoelectric conversion processes in OSCs, including exciton formation, charge generation, transport, and extraction, occur almost entirely within the active layer. Consequently, the morphology of the active layer critically bridges photophysical processes and device performance, playing a decisive role in performance optimization.[25-30] Althoug processing methods like solvent/additive selection, thermal annealing, or solvent vapor annealing can modulate phase evolution, the principle governing factors remain the intrinsic aggregation behaviors of the active materials, donor-acceptor interactions, and film-formation kinetics.[31, 32] For instance, weak polymer aggregation in solution yields highly dispersed polymer chains, which raises the crystallization barrier[33, 34] and persists in the solid-state, thereby impeding the formation of an ordered fibrillar network. Conversely, excessive aggregation can induce severe donor-acceptor phase separation during film formation, resulting in excessively large domains and poor exciton dissociation.[33, 34] High-performance BDTT-based conjugated polymers usually exhibit controllable pre-aggregation in solution, as evidenced by temperature-dependent absorption spectroscopy.[17, 35] The tailored aggregation is maintained in the solid state, promoting the formation of rope-like polymer semicrystals. Therefore, precise control of conjugated polymer aggregation in solution is essential for optimizing the solid-state active layer morphology and achieving high-performance OSCs.

Polymer aggregation is governed by interchain interactions. While alkyl chain engineering can modulate these interactions and adjust aggregation strength,[36, 37] the inherent flexibility and conformational disorder of carbon–carbon single bonds often disrupt polymer packing, reduce molecular orientation, and degrade crystallinity and charge transport. An alternative strategy involves direct backbone modification. Introducing fluorine atoms, leveraging their small atomic radius and high electronegativity, is an efficient

strategy to tune energy levels, improve backbone planarity, and strengthen intra- and intermolecular interactions.[38, 39] Despite these advantages, fluorination faces practical limitations including low synthesis yields, difficulties in byproducts removal, and high costs. Chlorination offers a more viable pathway.[40, 41] Chlorine atoms can be incorporated into backbones more readily at lower cost,[40, 42, 43] and their moderate Pauling electronegativity help deepen the highest occupied molecular orbital (HOMO) levels, thereby optimizing donor-acceptor energy level alignment. Crucially, the vacant 3*d*-orbitals of chlorine enable non-covalent interactions (e.g. Cl···π, Cl···S),[40] allowing fine regulation over polymer aggregation and donor-acceptor compatibility.

Building on our previous development of high-performance, thiazolothiazole-based linear conjugated polymer donors featuring temperature-dependent aggregation characteristics,[44, 45] this study demonstrates precise modulation of polymer aggregation behavior through strategic backbone chlorination. We design a series of linear conjugated polymers (PTTz-Cl*x*, where x = 0, 50, 100) by incorporating varying proportions of 3,4-dichlorothiophene (2ClT). These polymers are efficiently synthesized from low-cost starting materials in only seven to nine reaction steps. Increasing the 2ClT content systematically enhances polymer aggregation, raises surface tension, and reduces thermodynamic compatibility with the acceptor BTP-eC9. Among them, PTTz-Cl50 exhibites optimal aggregation strength and donor-acceptor compatibility, effectively regulating phase separation kinetics during film formation. This results in a well-defined bicontinuous interpenetrating network with appropriate domain size and high phase purity. The optimized morphology gives a balanced exciton dissociation, charge transport, extraction, and recombination suppression. As a result, PTTz-Cl50-based devices achieve a PCE of 20.42%, which is a high value for linear conjugated polymer-based OSCs. This work elucidates how aggregation behavior and donor-acceptor compatibility govern film formation kinetics and active layer morphology. It further reveals that the performance gap with BDTT-based polymers originates from the formation of optimally sized pre-aggregates in solution. Deeper insight into this structure-property-performance relationship is essential for rationally designing high-performance yet low-cost conjugated polymers and will accelerate the commercialization of organic photovoltaics.

Results

Polymer design and properties

The chemical structures of the PTTz-Cl*x* polymers are shown in Fig. 1a, with synthetic routes detailed in Supplementary Fig. 2. The key monomer 2ClT-Sn was synthesized in two steps with a high overall yield. The target polymers were obtained in only seven to nine total synthetic steps, which demonstrates significantly lower synthetic complexity than BDTT-based polymers.[12-14, 35] Gel permeation chromatography (GPC) analysis (Supplementary Fig. 3) reveals similar number-average molecular weights (M_n) and dispersity ($Đ_M$) values across the polymers, which minimizes the potential impacts of molecular weight on aggregation, morphology, and device performance. All polymers exhibit excellent solubility in common organic solvents such as chloroform, chlorobenzene, *o*-dichlorobenzene, enabling solution-processed device fabrication. Thermogravimetric analysis (TGA) confirms sufficient thermal stability, with 5% weight loss temperatures (T_d) exceeding 400 °C for all polymers (Supplementary Fig. 4). In contrast to BDTT-based polymers, differential scanning calorimetry (DSC) reveals distinct melting and crystallization peaks of these linear conjugated polymers (Supplementary Fig. 5), indicating an ordered molecular arrangement. Both melting (T_m) and crystallization temperature (T_c) increase progressively with 2ClT content. Specifically, T_m rises from 279 °C (PTTz-Cl0) to 293 °C (PTTz-Cl50) and further to 327 °C (PTTz-Cl100), while T_c increases from 275 °C to 279 °C and then to 298 °C, respectively, suggesting enhanced crystallinity upon chlorination. Although higher crystallinity generally favors charge transport, hole mobilities (μ_h) measured by the space-charge-limited-current (SCLC) method increase only moderately, from 1.68×10^{-3} cm^2 V^{-1} s^{-1} for PTTz-Cl0 to 1.82×10^{-3} cm^2 V^{-1} s^{-1} for PTTz-Cl50 and 2.20×10^{-3} cm^2 V^{-1} s^{-1} for PTTz-Cl100 (Supplementary Fig. 6). This limited enhancement can be attributed to the changes in molecular orientation, as is discussed in the following section.

Ultraviolet-visible (UV-Vis) absorption spectra of the polymer solutions in chloroform and as thin films are presented in Supplementary Fig. 7. In solution, all polymers absorb in the 300–650 nm range, showing distinct peaks attributed to intramolecular charge transfer (ICT) transitions along with associated vibronic progressions, labeled as the main peak (A_{0-1}) and the shoulder (A_{0-0}), respectively.[46, 47] Notably, increasing

the 2ClT content progressively enhances the intensity and induces a bathochromic shift of the $A_{0\text{-}0}$ shoulder, indicating a more ordered molecular packing,[48] which stems from the enhanced interchain interactions and significant solution-phase pre-aggregation.[49-51] Similar trends are observed in the solid-state spectra, suggesting that the ordered molecular stacking is preserved from solutions to film.[49-51] All polymer films exhibit absorption onsets (λ_{onset}) around 650 nm, corresponding to optical bandgaps (E_g^{opt}) of approximately 1.90 eV (Supplementary Table 1), which complement the absorption profiles of efficient Y6 derivatives. Furthermore, cyclic voltammetry (CV) measurements reveal progressively downshifted lowest unoccupied molecular orbital (LUMO) and HOMO energy levels with increasing 2ClT content (Supplementary Fig. 8), consistent with the electron-withdrawing effect of chlorine.

To probe the impact of 2ClT incorporation on molecular conformation and electronic properties, we conduct density functional theory (DFT) calculations.[52] Methyl-substituted tetramers were employed to model the polymer backbones. As illustrated in Supplementary Fig. 9, all polymers exhibit planar backbones, which facilitate intramolecular electron delocalization and strengthen interchain π–π stacking, thereby benefiting charge transport. The LUMO/HOMO wavefunctions are both delocalized along the molecular backbone (Supplementary Fig. 10). The computed LUMO/HOMO levels decrease systematically from –2.92/–5.08 eV for PTTz-Cl0 to –3.01/–5.16 eV for PTTz-Cl50 and –3.08/–5.25 eV for PTTz-Cl100, aligning well with the CV measurements. The experimentally and computationally confirmed downshifted HOMO levels are expected to contribute to a higher open-circuit voltage (V_{oc}) in devices. The DFT-calculated intramolecular Cl···S distance (3.19 Å) is significantly shorter than the sum of their van der Waals radii (3.55 Å),[53, 54] suggesting the presence of Cl···S non-covalent interactions (NCIs). We quantified NCI strength using the descriptor *S*, which correlates with molecular planarity, orbital angles, and atomic distances.[55] As proposed by Liu et al., an *S* value ≥ 0.14 indicates effective NCIs. Analysis at two backbone positions for each polymer (Supplementary Fig. 9 and Supplementary Table 2) revealed clear trends. PTTz-Cl0 shows negligible *S* values, indicating no effective intramolecular NCIs. PTTz-Cl50 exhibits localized effective NCIs (S = 0.003 at position 3 and S = 0.175 at position 4). PTTz-Cl100 displays robust *S* values (0.174 and 0.178) at both positions, confirming prevalent intramolecular NCIs. These pronounced Cl···S

interactions in chlorinated polymers should enhance backbone planarity and improve conformational stability.

To validate the impact of Cl···S interactions on polymer conformation and intra-/intermolecular packing, we grew single crystals of model compounds 2,2':5',2''-terthiophene (3T) and 3',4'-dichloro-2,2':5',2''-terthiophene (3T-Cl) via liquid diffusion for X-ray diffraction analysis. The quality of the crystal structures is validated using checkCIF (Supplementary Figs. 11-12 and Supplementary Datas 1-2). The refined crystal structures (Fig. 1b, Supplementary Table 3) show that both molecules adopt nearly planar configurations with small torsion angles. Compound 3T exhibits two distinct conformations, with thiophene units adopting contralateral orientations and slightly different dihedral angles (Supplementary Table 4). The intramolecular H···S distance in 3T (2.95 ± 0.1 Å) is close to the sum of van der Waals radii (3.00 Å), indicating no significant NCI. Adjacent 3T molecules adopt a slipped packing mode without discernible π–π interactions. In contrast, the intramolecular Cl···S distance in 3T-Cl (3.19 Å) is significantly shorter than the sum of van der Waals radii (3.55 Å), confirming a strong intramolecular NCI. This interaction stabilizes a single molecular conformation in 3T-Cl and promotes face-to-face packing with a π–π stacking distance of 3.57 Å, highlighting enhanced conformational stability and strengthened intermolecular interactions.

Polymer aggregation in solution

Polymer aggregation behaviors were probed by temperature-dependent UV-vis absorption spectrascopy in dilute chlorobenzene solutions (Fig. 1c). As the temperature increases from 25 to 95 °C, all polymers show a gradual decrease in the $A_{0\text{-}0}$ peak intensity along with a blue shift of the $A_{0\text{-}1}$ peak, confirming their temperature-dependent aggregation characteristics. For PTTz-Cl0, the $A_{0\text{-}0}$ peak vanishes completely at 85 °C, whereas PTTz-Cl50 retains this peak even at 95 °C, indicating stronger interchain interactions induced by chlorination. Predictably, PTTz-Cl100 shows minimal spectral changes, consistent with robust aggregation (Fig. 1d). Dynamic light scattering (DLS) in chloroform further supports these trends, showing hydrodynamic diameters (Z-average size) of 357.9 nm for PTTz-Cl0, 483.5 nm for PTTz-Cl50, and 519.8

nm for PTTz-Cl100 (Supplementary Fig. 13). Among the series, PTTz-Cl50 exhibits a suitable pre-aggregation strength, favorable for optimizing active layer morphology in devices.[56]

To understand the performance gap between linear conjugated polymers and high-performance BDTT-based polymers, we compared the solution-state aggregation of the designed polymers with the conventional linear conjugated polymer P3HT[26] and the high-performance BDTT-based polymer D18[13] by small-angle neutron scattering (SANS). Given that PTTz-Cl0 still exhibits notable temperature-dependent aggregation, we specifically synthesized another control polymer 4HD-Cl50 (Supplementary Fig. 14), which shares the same backbone and chlorination degree with PTTz-Cl50 but features an altered alkyl chain position, introducing steric hindrance and thereby molecular twisting. The SANS data (Fig. 1e and Supplementary Fig. 15) are well fitted using a cylinder model based on the Guinier–Porod approximation,[57] yielding the radius (R) and contour length (L) of the pre-aggregates. Both R and L increase progressively with chlorination, from 27.9/275 Å for PTTz-Cl0 to 32.4/304 Å for PTTz-Cl50, and further to 46.0/337 Å for PTTz-Cl100 (Supplementary Fig. 16). The radius of gyration (R_g), reflecting the overall size of the scattering objects, is calculated as $R_g^2=L^2/12+R^2/2$. The R_g values also rise consistently, from 81.8 Å to 90.7 Å and finally to 102.6 Å, reflecting the formation of progressively larger pre-aggregates. Notably, the R_g values of the chlorinated polymers approach that of the high-performance polymer D18 (99.9 Å), whereas P3HT and the more twisted 4HD-Cl50 show smaller R_g values (60.9 Å and 56.7 Å), suggesting weaker aggregation propensity. Upon blending with the acceptor BTP-eC9, both L and R of the scattering objects increase, but to varying extents, revealing anisotropic growth of polymer assemblies. The axial ratio (L/R) is used to quantify this growth orientation. As illustrated in Supplementary Fig. 17, the PTTz-Clx series and D18 blends exhibit similar ratios around 10, while 4HD-Cl50 and P3HT show higher ratios that are increased by nearly 50%. These results indicate that strongly aggregating linear conjugated polymers tend to form thicker fibers, resembling those in high-performance D18, whereas weakly aggregating counterparts tend to form wispy fibrous structures. Critically, these solution-phase fibrous assemblies can be carried over into solid-state, ultimately governing the active layer morphology and thereby device performance.

Molecular packing and arrangement

Two-dimensional grazing-incidence wide-angle X-ray scattering (2D-GIWAXS) was employed to characterize molecular packing in neat polymer films.[58, 59] The 2D-GIWAXS patterns and corresponding one-dimensional line-cut profiles are presented in Figs. 2a-b, with relevant lattice parameters summarized in Supplementary Table 5-6. All polymers exhibit distinct out-of-plane (OOP) (010) π–π stacking peaks and (h00) lamellar diffractions, along with concurrent in-plane (IP) (010) and (100) peaks, indicating mixed face-on and edge-on orientations. With increasing 2ClT content, diffraction intensities shift systematically. OOP (010) intensity decreases while (100) increases, and the reverse trend is observed in the IP direction, suggesting a gradual transition from face-on to edge-on orientation. This shift stems from enhanced intermolecular interactions, which promote preferential chain-chain interactions over chain-substrate interactions, leading to more pronounced edge-on orientation in neat films.[60-63] The edge-on orientation impedes charge transport perpendicular to the substrate, resulting in a trade-off between molecular orientation and crystallinity that yields no significant improvement in hole mobility. The non-linear variation in (010) peak position with chlorine content may be associated with the ternary random copolymerization in PTTz-Cl50. To quantify the evolution in molecular orientation, pole figures of the (010) and (100) diffraction peaks are analyzed. For the (010) peaks, the face-on population (A_z) integrates the sin-corrected intensities within (–45°, 45°), while the edge-on population (A_{xy}) covers ±(45°, 90°). The azimuthal intensity distribution reveals nearly constant face-on fractions but substantially increased edge-on fractions with 2ClT content (Fig. 2c). The A_z/A_{xy} ratio decreases from 4.24 for PTTz-Cl0 to 1.25 for PTTz-Cl50 and 0.31 for PTTz-Cl100, corresponding to a reduction in face-on π–π stacking population from 81% to 56% and further to 24% (Fig. 2d). Additionally, higher 2ClT content enhances polymer crystallinity, as is evidenced by increased diffraction peak intensities and integrated areas for the same crystallographic planes. The relative degree of crystallinity (rDoC), proportional to the integrated GIWAXS intensity, quantifies the crystalline volume fraction within the films.[58] The rDoC derived from the integrated intensity of the (010) pole figures, increases from 9.24 for PTTz-Cl0 to 15.03 for PTTz-Cl50 and 38.63 for PTTz-

Cl100 (Supplementary Fig. 18 and Supplementary Table 7), demonstrating a significant enhancement in crystallinity. A similar trend is observed for the (100) lamellar stacking (Supplementary Fig. 19, Supplementary Table 7). Importantly, PTTz-Cl50 exhibits moderate crystallinity in both π–π and lamellar directions, enabling efficient charge transport while avoiding excessive crystallization during film formation. In polymer:acceptor blends, all systems display distinct OOP (010) π–π stacking and prominent IP (100) lamellar peaks (Supplementary Fig. 20 and Supplementary Table 8), indicating a dominant face-on orientation. Although the neat polymer films exhibit bimodal orientation, the edge-on population reorients to a face-on configuration in the blends, likely due to polymer-acceptor π-π interactions and reduced π-stacking strength of the polymers in the presence of the acceptor.[60, 64] Such face-on orientation facilitates efficient charge transport perpendicular to the substrate.

Morphology analysis

To understand how polymer aggregation and crystallinity influence blend film microstructure, we characterized the morphology of the blend films processed from chloroform with 0.5 vol% diphenyl ether (DPE) using transmission electron microscopy (TEM) and atomic force microscopy (AFM). TEM images (Figs. 3a-c) reveals a relatively homogeneous morphology for the PTTz-Cl0:BTP-eC9 blend. In contrast, PTTz-Cl50:BTP-eC9 exhibits a well-defined fibrillar network structure, similar to the high-performance D18:BTP-eC9 reference (Supplementary Fig. 21),[65] indicating appropriate phase separation conducive to device performance. The PTTz-Cl100:BTP-eC9 blend, however, displays strong bright/dark contrast in TEM, reflecting excessive phase separation and overly large domains that reduce donor/acceptor interfacial area and impair exciton dissociation. For the weakly aggregated polymers 4HD-Cl50 and P3HT, their higher solubility likely promots liquid-liquid phase separation during film formation, leading to coarse domains with large bright and dark regions (Supplementary Fig. 21). AFM height images (Figs. 3d-f) are consistent with this trend. The PTTz-Cl0:BTP-eC9 blend has a smooth surface with a root-mean-square (RMS) roughness of 1.47 nm, while roughness increases slightly to 1.73 nm for PTTz-Cl50:BTP-eC9 and further to 2.41 nm for PTTz-Cl100:BTP-eC9. All the blends develop fine fibrillar networks (Supplementary

Fig. 22), resembling the morphology of the D18-based blend (Supplementary Fig. 23). By comparison, 4HD-Cl50:BTP-eC9 and P3HT:BTP-eC9 blends exhibit noticeable pits or protrusions in AFM height images (Supplementary Fig. 23), likely due to liquid-liquid phase separation and large differences in solid-state density between the polymer donor and small-molecule acceptor. These distinct morphological outcomes underscore how aggregation and crystallinity govern active layer structure, ultimately dictating the device performance differences observed among linear conjugated polymers and BDTT-based polymers.

To directly visualize the distribution of nanoscale donor and acceptor phases, atomic force microscopy-infrared spectroscopy (AFM-IR) mapping were performed (Figs. 3g-i),[66] employing the characteristic BTP-eC9 absorption peak at 1,364 cm^{-1} (Supplementary Fig. 24) for identification. In the PTTz-Cl0:BTP-eC9 blend, a largely intermixed morphology (red regions) is observed, providing ample donor/acceptor interfaces favorable for exciton dissociation. The PTTz-Cl50:BTP-eC9 blend develops slightly enlarged and purified acceptor domains, forming an interpenetrating fibrillar network with well-defined phases separation, a structure conducive to both efficient exciton dissociation and continuous charge transport. Conversely, PTTz-Cl100:BTP-eC9 shows excessive phase separation with overly large domains, which significantly reduce the interfacial area and impair exciton dissociation. To determine the origin of these distinct bulk heterojunction (BHJ) morphological differences, we evaluate the thermodynamic compatibility between polymer donors and BTP-eC9 using the Flory-Huggins interaction parameter (χ).[67] Contact angle measurements with water and ethylene glycol on pristine polymer and BTP-eC9 films are used to estimate χ values (Supplementary Fig. 25). Increasing the 2ClT content progressively increases contact angles on polymer surfaces, corresponding to a decrease in surface tension (Supplementary Table 9). The calculated χ values increase from 0.14 κ for PTTz-Cl0:BTP-eC9 to 0.17 κ for PTTz-Cl50:BTP-eC9 and 0.22 κ for PTTz-Cl100:BTP-eC9. The low χ value for PTTz-Cl0:BTP-eC9 signifies higher donor-acceptor compatibility, yielding a finely mixed phase. Moderate chlorination reduces compatibility, slightly enlarging domain size in PTTz-Cl50:BTP-eC9 blends, while excessive chlorination results in poor compatibility and oversized phase separation in PTTz-Cl100:BTP-eC9, consistently explaining the observed morphological trend.

Film-Formation Kinetics

In addition to thermodynamic factors, film-formation kinetics play a critical role in determining the final bulk-heterojunction morphology. To study the dynamic processes influenced by polymer aggregation, we first performe in-situ UV-vis-NIR absorption measurements on PTTz-Cl*x*:BTP-eC9 blends in chloroform (Supplementary Fig. 26). The polymer donors exhibit negligible spectral changes during film formation, indicating that strong pre-aggregation has already formed in solution and is retained in the solid state, ultimately contributing to a continuous polymer network. In contrast, the acceptor BTP-eC9 displays notable spectral evolution as the solvent dried. Based on variations in absorption intensity and peak position, the film formation process can be divided into three distinct stages: a dissolved state (S1), nucleation and growth (S2), and solid-film formation (S3).[68, 69] During S1, dominated by the evaporation of chloroform, the absorption profile of BTP-eC9 remains nearly unchanged. In S2, continued solvent loss induces supersaturation and acceptor precipitation,[69] accompanied by a drop in absorption intensity and a red-shift of the absorption peak. S3 corresponds to the final solid film with stabilized spectral characteristics. As shown in Supplementary Fig. 26, all blends undergo rapid nucleation and growth within 1 second, with PTTz-Cl50 exhibiting a slightly extended crystallization period.

Under device fabrication conditions (CF with 0.5 vol% DPE), as the primary solvent evaporation concluds, the high-boiling additive DPE promots further acceptor reorganization, enhancing molecular ordering and inducing an additional red shift (Figs. 4a-c and Supplementary Fig. 27). This step is designated as S2a. As shown in Fig. 4d, in the highly compatible PTTz-Cl0:BTP-eC9 system, S1 lasts 1 second, followed by rapid concurrent donor-acceptor solidification during S2 and S2a (0.89 seconds total), leaving little time for molecular reorganization and resulting in mixed phases. For PTTz-Cl50:BTP-eC9, the prolonged S2 stage (1.44 seconds) enables synchronous donor-acceptor assembly, promoting adequate interfacial contact. Subsequent DPE-assisted ordering in S2a supports the formation of continuous and ordered acceptor domains (Fig. 4e). In the poorly compatible PTTz-Cl100:BTP-eC9 system, strong polymer aggregation drives rapid solidification within ~1 second (Fig. 4f), while low compatibility causes

the precipitating donor to expel the acceptor. Subsequent DPE-induced ordering of the isolated acceptor then forms oversized, high-purity domains, which detrimentally hinder exciton dissociation and charge extraction, ultimately degrading device performance. Therefore, synergistic control of polymer aggregation and film-formation kinetics is essential to achieving an optimal active layer morphology (Fig. 4g). Appropriate polymer aggregation promotes well-ordered pre-aggregates of optimal size in solution, which persist into the solid film. Suitable donor-acceptor compatibility enables controlled deposition and ordered assembly of both components during film formation, preventing excessive mixing while avoiding oversized domains caused by rapid solidification.

Photovoltaic performance

The photovoltaic performance of the synthesized polymers are assessed in conventional architecture OSCs. A comprehensive device optimization is undertaken by systematically varying fabrication conditions. The current density versus voltage (*J*–*V*) characteristics for the best-performing devices are displayed in Fig. 5a, with the corresponding photovoltaic parameters summarized in Table 1. The PTTz-Cl0-based device achieves a PCE of 17.30%, with a V_{oc} of 0.826 V, a J_{sc} of 27.27 mA cm^{-2}, and an FF of 76.83%, which is better than our previously reported value as a result of optimized fabrication conditions.[44] Notably, the PTTz-Cl50-based device yields a PCE of 20.42%, accompanied by a V_{oc} of 0.856 V, a J_{sc} of 29.79 mA cm^{-2}, and an FF of 80.13%. The external quantum efficiency (EQE) spectrum of the PTTz-Cl50-based device exhibits significant enhancement across 450–850 nm (Fig. 5b), covering both donor and acceptor absorption regions, indicating superior photon utilization. The integrated J_{sc} of the optimal device agrees well with the *J*–*V* measurement. We also characterized the internal quantum efficiency (IQE) of the champion device and the substrate transmittance (Supplementary Fig. 28), confirming the reliability of the EQE data. This efficiency represents a high value for OSCs based on linear conjugated polymer donors to date (Fig. 5c, Supplementary Tables 10-14). The V_{oc} enhancement primarily results from the deeper-lying HOMO level of PTTz-Cl50, while concurrent improvements in J_{sc} and FF are ascribed to the finely improved active layer morphology. However, further increasing the 2ClT content to 100% yields a reduced PCE of 15.35%.

Although the V_{oc} slightly increases to 0.866 V, both the J_{sc} (25.95 mA cm^{-2}) and FF (69.72%) drop dramatically, ultimately compromising overall device performance. Likewise, devices based on 4HD-Cl50:BTP-eC9 and P3HT:BTP-eC9 exhibit inferior performance (Supplementary Table 15).

To gain deeper insight into the V_{oc} characteristics, we analyzed energy loss (ΔE_{loss}) via highly sensitive EQE and electroluminescence (EL) measurements (Supplementary Fig. 29). According to Shockley-Queisser (SQ) limit theory, the total E_{loss} in OSCs is composed of ΔE_1 (intrinsic radiative recombination loss), ΔE_2 (radiative loss from sub-bandgap states), and ΔE_3 (non-radiative recombination loss, calculated as $-k_BT\ln(EQE_{EL})$). While ΔE_1 is similar across all devices, the PTTz-Cl50-based device exhibits the smallest ΔE_2 (0.040 eV), compared to PTTz-Cl0 (0.052 eV) and PTTz-Cl100 (0.051 eV). Moreover, the chlorinated systems exhibit higher EQE_{EL} values than the non-chlorinated PTTz-Cl0 counterpart (Supplementary Fig. 30a). This enhancement leads to a corresponding reduction in ΔE_3 from 0.244 eV (PTTz-Cl0) to 0.214 eV (PTTz-Cl50) and 0.200 eV (PTTz-Cl100), as shown in Supplementary Fig. 30b and Supplementary Table 16. The concurrent suppression of ΔE_2 and ΔE_3 thus accounts for the higher V_{oc} values in chlorinated polymer-based devices. Beyond efficiency, the operational stability of the optimal PTTz-Cl50-based device against the D18 reference is evaluated by tracking the maximum power point (MPP) under simulated 1-sun white-light illumination. After 400 hours of continuous illumination, the PTTz-Cl50-based device retains 80% of its initial efficiency, whereas the D18-based counterpart loses over 30% (Supplementary Figs. 31-32), highlighting the potential of the developed linear conjugated polymers for achieving both high efficiency and excellent stability. Besides, device performance with *o*-xylene and CS_2 in a 1:1 volume ratio as solvent shows performance comparable to those using chloroform (Supplementary Fig. 33, Supplementary Table 17), demonstrating suitability for green-solvent and large-scale processing. Given the simple structure and outstanding photovoltaic performance, we further assesse the synthetic accessibility of PTTz-Cl*x* polymers via synthetic complexity (SC) analysis (Supplementary Table 18-19). The SC values are 38.68%, 47.05%, and 42.6% for PTTz-Cl0, PTTz-C50, and PTTz-Cl100, respectively. Although PTTz-Cl50 involves three comonomers and shows slightly higher synthetic

complexity, its SC remains lower than that of benchmark BDTT-based polymers (e.g., D18: 81.70%, PBQx-TF: 78.59%, PM6: 68.91%, PB2F: 75.17%). We further calculate the figure of merit (FOM = PCE/SC). PTTz-Cl0 and PTTz-Cl50 achieve exceptional FOMs of 0.45 and 0.43, respectively, significantly surpassing BDTT-based polymers (e.g., D18: 0.25, PBQx-TF: 0.25, PM6: 0.29, PB2F: 0.25). This favorable balance between synthetic accessibility and high efficiency renders PTTz-Cl50 exceptionally promising for practical applications.

Charge carrier dynamics

To elucidate the mechanism behind the enhanced photovoltaic performance, we investigate the charge transfer characteristics of the blend films using steady-state photoluminescence (PL) quenching measurements. All PTTz-Cl*x*:BTP-eC9 blend films exhibit over 99% donor quenching efficiencies (Supplementary Fig. 34). The acceptor quenching efficiency slightly decreases to 96% for PTTz-Cl50:BTP-eC9 (98% for PTTz-Cl0:BTP-eC9), but severely to 90% for PTTz-Cl100:BTP-eC9 (Supplementary Fig. 35 and Supplementary Table 20). The diminished acceptor quenching efficiency suggests reduced dissociation of acceptor-generated excitons and hindered hole transfer to the donor, likely stemming from enlarged acceptor aggregates. The exciton dissociation probability (P_{diss}) within operational devices, determined from photocurrent density versus effective voltage plots,[70] corroborates this trend (Supplementary Fig. 36). Regarding charge transport, all blends exhibit hole mobility comparable to their pure counterparts (Fig. 5d). Electron mobilities in the blends increase with 2ClT content, attributed to the formation of continuous transport pathway. The μ_h/μ_e ratios are 1.18 for PTTz-Cl0:BTP-eC9, 1.04 for PTTz-Cl50:BTP-eC9, and 0.55 for PTTz-Cl100:BTP-eC9. The charge transport imbalance in PTTz-Cl100:BTP-eC9 likely contributes to charge accumulation and recombination, thereby degrading device performance.

To elucidate the dominant charge recombination mechanisms in the devices, we examine the dependence of the V_{oc} on light intensity.[71-73] The slope of this relationship, characterized by an ideality factor n, helps distinguish between recombination pathways. A value of $n \sim 1$ is indicative of bimolecular

recombination being predominant,[71] whereas *n* approaching 2 suggests that trap-assisted recombination is the primary loss mechanism.[72, 73] As shown in Fig. 5e, the extracted *n* values are 1.16, 1.11 and 1.27 for PTTz-Cl0-, PTTz-Cl50-, and PTTz-Cl100-based devices, respectively. The lower *n* values for PTTz-Cl0- and PTTz-Cl50-based device confirm suppressed trap-assisted recombination. Transient photovoltage (TPV) measurements provided further insight into carrier dynamics. Fig. 5f shows that the photocarrier lifetimes (τ_{rec}) is prolonged in the PTTz-Cl50-based device (31.97 μs) compared to PTTz-Cl0- (27.92 μs) and PTTz-Cl100-based device (22.36 μs), directly evidencing suppressed charge recombination. Moreover, the PTTz-Cl50 device exhibits the shortest charge extraction time (τ_{ext} = 0.137 μs), shorter than those of PTTz-Cl0 (0.160 μs) and PTTz-Cl100 (0.212 μs) (Fig. 5g), signifying more efficient charge collection.[74] In summary, the superior J_{sc} and FF observed for the PTTz-Cl50-based device arise synergistically from the efficient exciton dissociation, rapid and balanced charge transport, suppressed recombination, and accelerated charge extraction.

To elucidate the superior performance of the PTTz-Cl50 device, we characterize the trap density in the active layers via capacitance–voltage (*C*–*V*) measurements and Mott-Schottky analysis.[75] In the linear Mott-Shockley regime (C^{-2}–*V*), the slope corresponds to the trap density (N_A) and the intercept to the built-in voltage (V_{bi}). N_A is calculated using Equation 1:

$$N_A = \frac{-2}{q\varepsilon_r\varepsilon_0 A^2}\left(\frac{dV}{dC^{-2}}\right) \quad (1)$$

where ε_r is the relative dielectric constant (assumed as 3 for organic semiconductors), ε_0 is the vacuum permittivity, and *A* is the device area. Fig. 5h shows a slightly steeper slope for PTTz-Cl50 than PTTz-Cl0, but a shallower slope for PTTz-Cl100. Consequently, N_A decreases from 1.22×10^{16} cm^{-3} (PTTz-Cl0) to 1.03×10^{16} cm^{-3} (PTTz-Cl50), then increased to 1.95×10^{16} cm^{-3} (PTTz-Cl100) (Supplementary Fig. 37 and Supplementary Table 22). This indicates that appropriate backbone chlorination reduces trap density, while excessive chlorination elevates it. The depletion width (*W*), derived from N_A and V_{bi} via Equation 2:[76]

$$W = \sqrt{\frac{2\varepsilon_r\varepsilon_0(V_{bi})}{qN_A}} \quad (2)$$

is largest for PTTz-Cl50 (165 nm), exceeding those for PTTz-Cl0 (152 nm) and PTTz-Cl100 (129 nm). This extended depletion width confirms full depletion across the entire active layer in the PTTz-Cl0- and PTTz-Cl50-based OSCs, but not in PTTz-Cl100-based device. Capacitance–frequency (*C*–*f*) measurements are further conducted to probe the density of states (DOS) distribution within the active layer.[77] Trap energy (E_ω), which is frequency-dependent as $E_\omega = kT\ln(\omega_0/\omega)$ with $\omega_0 = 10^{12}$ s^{-1},[78] allows extraction of the trap DOS using Equation 3:

$$\mathrm{DOS}(E_\omega) = \frac{N_G}{\sigma\sqrt{2\pi}}\exp\left(-\frac{(E_\omega - E_{G0})^2}{2\sigma^2}\right) \quad (3)$$

Single Gaussian fitting reveals superior trap characteristics for PTTz-Cl50-based OSC (Fig. 5i, Supplementary Fig. 38, Supplementary Table 23). Its trap density ($N_t = 2.22 \times 10^{14}$ cm^{-3}) is lower than those of the OSCs based on PTTz-Cl0 (6.52×10^{14} cm^{-3}) and PTTz-Cl100 (6.93×10^{14} cm^{-3}). The PTTz-Cl50-based device also exhibits the shallowest mean trap energy ($E_t = 0.36$ eV) and narrowest Gaussian disorder width ($\sigma = 30$ meV). These favorable properties minimize carrier trapping while facilitating de-trapping, thereby suppressing recombination and enhancing J_{sc} and FF.

The excited-state behaviors of the blends are investigated by transient absorption (TA) spectroscopy (Figs. 6a-c). The TA spectra acquired over a nanosecond timescale used an 800 nm pump wavelength to selectively excite the acceptor (BTP-eC9). Following excitation, a decrease in the acceptor ground-state population appears as negative signal bands symmetrically aligned with its steady-state absorption features in the 810–870 nm region, assigned to acceptor ground-state bleach (GSB). This GSB signal decays as the acceptor relaxes to its ground state. Notably, negative signals also emerge in the 500–650 nm range, corresponding to donor GSB. As excitation was selective to the acceptor, the donor GSB signals arises exclusively from hole transfer from the excited acceptor to the donor. Thus, the donor GSB signal intensity directly indicates hole transfer efficiency. The PTTz-Cl0:BTP-eC9 blend exhibits the most intense donor GSB signal (Figs. 6d-f), indicating the most efficient hole transfer. This high efficiency is attributed to excellent D/A compatibility, which facilitates ample D/A interface formation, enabling effective exciton dissociation into free charges and efficient hole transfer to the donor. Excitons generated distal to D/A

interfaces dissociate less efficiently, deteriorating charge transfer. This is reflected in the progressively diminished donor GSB signal intensity with higher chlorination levels.

By extracting the GSB kinetics at 820 and 610 nm, the hole transfer dynamics are analyzed (Figs. 6g–i). The kinetic traces reveal an instantaneous peak in acceptor GSB post-excitation, concomitant with a sharp rise in donor GSB. This immediate response signifies ultrafast exciton dissociation and direct hole transfer at the donor/acceptor interfaces. Subsequently, the acceptor signal decays gradually while the donor signal exhibits a slow, continuous increase. This slower component originates from diffusion-mediated exciton dissociation and charge transfer. Therefore, the hole transfer process comprises two distinct pathways: an ultrafast interface-driven process and a slower diffusion-mediated process. These kinetics are modeled using a biexponential function:

$$I = A_1\left(1 - e^{\frac{-t}{\tau_1}}\right) + A_2\left(1 - e^{\frac{-t}{\tau_2}}\right) \quad (4)$$

where τ_1 represents the ultrafast interfacial hole transfer lifetime and τ_2 denotes the lifetime of the diffusion-mediated process, governed by domain size. Typically, longer τ_2 indicates larger phase separation scales. As summarized in Supplementary Table 24, all blends exhibit comparable τ_1 values (0.4 ± 0.1 ps), suggesting similar ultrafast exciton dissociation kinetics at the donor/acceptor interface. The τ_2 for PTTz-Cl0:BTP-eC9 (4.8 ps) is slightly shorter than that for PTTz-Cl50:BTP-eC9 (5.5 ps), consistent with its marginally refined morphology. In contrast, PTTz-Cl100:BTP-eC9 shows a substantially longer τ_2 (13.6 ps). This unambiguously demonstrates that enlarged acceptor domain sizes result from excessive chlorination of the polymer donors, which impede exciton dissociation.

Discussion

In summary, this study elucidates the performance gap between linear conjugated polymers and high-efficiency BDTT-based polymers, revealing that precise control of polymer aggregation and donor-acceptor compatibility governs film-formation kinetics and active layer morphology. By incorporating the 2ClT unit into the linear conjugated polymer backbone, Cl···S non-covalent interactions promote polymer pre-aggregation and enhance crystallinity. Concurrently, increased chlorination lowers the polymer surface

energy, thereby reducing its compatibility with the non-fullerene acceptor. The designed polymer PTTz-Cl50 achieves a balance between aggregation tendency and acceptor compatibility, which facilitates sequential crystallization of the donor and acceptor, leading to an optimal bi-continuous fibrillar network morphology. This morphology promotes rapid charge generation, balanced charge transport, and suppressed recombination, ultimately enabling OSCs based on PTTz-Cl50 to achieve an outstanding PCE of 20.42%. These findings highlight how deliberate molecular design can steer film formation and morphology to achieve high performance in cost-effective OSC systems, enhancing the potential of simple linear conjugated polymers as efficient donor materials for low-cost photovoltaic applications.

Methods

Gel permeation chromatography (GPC): The molecular weights of the polymers were determined using an Agilent Technologies PL-GPC 220 high-temperature chromatography in 1,2,4-trichlorobenzene (TCB) at 150 °C against a calibration curve of polystyrene standards.

Thermogravimetric analyses (TGA): TGA measurements were conducted with a NETZSCH (TG209F3) apparatus at a heating rate of 20 °C min^{-1} under a nitrogen atmosphere.

Differential scanning calorimetry (DSC): DSC measurements were performed on a NETZSCH DSC200F3 apparatus under a nitrogen atmosphere. The first cycle used heating/cooling rates of 10/20 °C min^{-1}, and the second cycle used rates of 10/40 °C min^{-1}.

Density functional theory (DFT) calculation: Geometry optimizations and frontier molecular orbital calculations were performed using Gaussian at the B3LYP/6-31G (d, p) level. All alkyl chains were substituted with methyl groups to simplify the computations.

Single crystal X-ray diffraction: Single-crystals of 3T and 3T-Cl were grown via slow diffusion of ethanol (a poor solvent) into their chloroform solutions (a good solvent). A suitable crystal was selected and mounted on a Rigaku XtaLAB P2000 diffractometer. The crystal was maintained at 100 K during data

collection. After data reduction, the structure was solved using the Intrinsic Phasing method in ShelXT and refined using the least-squares minimization method in ShelXT.

UV-vis absorption spectra: UV-Vis absorption spectra of the polymers in chloroform solutions and as thin films were recorded on a SHIMADZU UV-3600 spectrophotometer. The solution concentration was 0.02 mg mL^{-1}. Thin films were prepared by spin-coating onto glass substrates.

Cyclic voltammetry (CV): CV measurements were conducted on a CHI660A electrochemical workstation using a 0.1 M solution of tetrabutylammonium hexafluorophosphate (Bu_4NPF_6,) in acetonitrile as the electrolyte. A glassy carbon electrode, a platinum wire, and an Ag/AgCl electrode served as the working, counter, and reference electrode, respectively. The ferrocene/ferrocenium (Fc/Fc^+) redox couple was used as an internal standard, with its absolute energy set to –4.80 eV relative to vacuum. The HOMO and LUMO energy levels were calculated using the following equations: $E_{HOMO} = -e(E_{ox\ onset} + 4.80 - E_{1/2}^{Fc/Fc+})$ and $E_{LUMO} = -e(E_{re,\ onset} + 4.80 - E_{1/2}^{Fc/Fc+})$, where $E_{ox,\ onset}$ and $E_{re,\ onset}$ are the onset potential for oxidation and reduction, respectively, referenced to the Fc/Fc^+ couple. The half-wave potential $E_{1/2}^{Fc/Fc+}$ was determined to be 0.42 V.

Dynamic Light Scattering (DLS): DLS was used to measure the size and size distribution of polymer aggregates in solutions. Measurements were performed using a HORIBA SZ-100Z instrument at 25 °C. Polymer samples were dissolved in chloroform at a concentration of 0.05 mg mL^{-1}.

Small-Angle Neutron Scattering (SANS): SANS experiments were conducted on the BL-2 (SANS) and BL-14 (VSANS) beamlines at the China Spallation Neutron Source (CSNS). For the VSANS beamline (BL-14), data were collected using neutron wavelengths ranging from 2.2 to 6.7 Å, with a collimation length of 12.75 m, providing a *q* range of 0.001-2.5 $Å^{-1}$. For the SANS beamline (BL-2), data were collected using neutron wavelength from 2 to 9.15 Å with a sample-to-detector distance of 5 m, covering a q range of 0.0045-0.375 $Å^{-1}$. The data were fitted using the SasView 5.0.6 software. Samples were prepared as solutions in $CDCl_3$ at concentrations of 7.0 mg mL^{-1} for PTTz-Cl*x*, 4HD-Cl50, P3HT, and 5.6 mg mL^{-1} for

D18. For donor:acceptor blends, a 1:1.2 weight ratio was used, matching the precursor solution for film deposition. All samples were loaded into quartz cells with a 2 mm path length, and scattering profiles were acquired at 25 °C.

Device fabrication: Patterned ITO glass substrates were cleaned sequentially by sonicating in detergent, deionized water at room temperature, followed by sonication in isopropanol bath. Each step lasted 15 minutes. The substrates were then treated with oxygen plasma for 5 minutes. A Ph-4PACz layer was then spin-coated onto the ITO substrates at 2000 rpm for 30 s, resulting in a thickness of ~5 nm, and then baked at 85 °C for 6 minutes. The substrates were then transferred into a nitrogen-filled glove box. The active layer (PTTz-Cl*x*:BTP-eC9) was deposited under the optimized conditions: a donor:acceptor ratio of 1:1.2 (w/w), a chloroform solvent containing 0.5 vol% diphenyl ether (DPE), and thermal annealing at 100 °C for 10 min. The resulting active layer thickness was approximately 135 nm. Subsequently, a PNDIT-F3N layer (~5 nm) was spin-coated from a solution in methanol/ethanol mixture (v/v = 1/3, 0.5 mg mL^{-1}) at 2000 rpm for 20 s. Finally, a 100 nm Ag electrode was thermally evaporated at a pressure of 5×10^{-6} Torr. For devices processed with non-halogenated solvents, the solvent was replaced with an o-xylene/CS_2 mixture (1:1, v/v), all other fabrication steps were identical. The evaporated Ag electrode defined a device area of 0.0516 cm^2. During testing, a steel mask was used to defined an accurate active area of 0.0324 cm^2.

Photovoltaic performance measurements: The photovoltaic performance was measured under AM1.5G irradiation (100 mW cm^{-2}) using a solar simulator (Enlitech, Taiwan). The light intensity was calibrated with a reference monocrystalline silicon solar cell (Enlitech) certified by the China General Certification Center. The current density–voltage (*J*–*V*) curves were recorded with a Keithley 2400 source meter.

External quantum efficiencies (EQEs): EQE spectra were measured using a QE system (QE-R3011, Enlitech, Taiwan). The light intensity was calibrated with a standard monocrystalline silicon photovoltaic cell (Enlitech).

Light-intensity dependence measurements: These measurements were performed under illumination intensities from 10 to 100 mW cm^{-2}. The light intensity was calibrated with a standard monocrystalline

silicon solar cell (Enlitech). The current density and voltage were recorded with a Keithley 2400 source meter.

Steady-state photoluminescence (PL): PL spectra were acquired using a Shimadzu RF-6000 spectrometer. Quenching efficiencies were determined by comparing the PL intensity of neat and blend films at their respective excitation wavelengths.

FTPS-EQE and EL-EQE measurements: FTPS-EQE was measured using an integrated system (PECT-600, Enlitech) with a lock-in amplifier. EL-EQE was measured by applying an external voltage/current to the devices using an REPS-Pro (Enlitech). All devices for EL-EQE were fabricated under optimal conditions. The applied voltage for EL-EQE range from 0 to 1.8 V.

Atomic force microscopy (AFM): AFM images were obtained using a Bruker Multimode 8 Microscope AFM in tapping mode.

Atomic force microscope-infrared spectroscopy (AFM-IR): AFM-IR images were acquired using a Bruker nanoIR3 in tapping-mode.

Transmission electron microscopy (TEM): TEM images were acquired using a JEM-2100F transmission electron microscope operated at 200 kV.

Grazing incidence wide-angle X-ray scattering (GIWAXS): GIWAXS measurements were performed on the 9A and 6D USAXS beamlines at the PLS-II, Korea. X-rays from an in-vacuum undulator (IVU) were monochromated to a wavelength of ~1.11 Å using a double-crystal monochromator and focused to 450 (H) × 60 (V) μm^2 (FWHM) at the sample position using K-B type mirrors. Scattering patterns were recorded with a 2D CCD detector (Rayonix SX165) using exposure time of 6−9 seconds, depending on the detector saturation. The diffraction angles were calibrated using a sucrose standard (monoclinic, P21, a = 10.8631 Å, b = 8.7044 Å, c = 7.7624 Å, β = 102.938 Å). The sample-to-detector distance was approximately 231 mm.

In-situ UV-vis absorption spectra: In situ UV-vis absorption spectra were recorded in transmission mode using an Ocean Optics QE Pro spectrometer with a time resolution of 0.5 s. The film formation process was monitored in reflection mode using a Filmetrics F20-EXR spectrometer with a time resolution of 0.04 s. Both measurements were performed on silicon substrates using the same precursor solutions as for device fabrication.

Fabrication and characterization of single-carrier devices: Hole-only devices with a structure of ITO/Ph-4PACz/active layer/MoO_3/Ag and electron-only devices with a structure of ITO/ZnO/active layer/PNDIT-F3N/Ag were fabricated. Charge carrier mobilities were extracted from the J_d–V characteristics, measured by applying a voltage from 0 to 4 V using a Keithley 2400 source meter.

Contact angle measurements: Contact angles were measured using a DataPhysics OCA40 Micro instrument. Samples were prepared by casting films onto Ph-4PACz-coated ITO substrates. Images were captured 60 s after droplet deposition. The surface tension was calculated from the contact angles of water and ethylene glycol using the Owens–Wendt–Kaelble (OW) method, where γ_d and γ_p represent the dispersive and polar components, respectively.

Femtosecond transient absorption characterization: TA measurements were performed using a home-built system. The system is driven by a commercial femtosecond laser amplifier (Legend Elite F 1K HE+II, Coherent) operating at 1 kHz, with a pulse duration of ~170 fs and a central wavelength of 800 nm, which is seeded by an 80 MHz oscillator (Mira-HP, Coherent). The output beam is split into two. One beam pumps a home-built non-collinear optical parametric amplifier (NOPA) to generate the tunable pump pulse. The pump beam is modulated at 500 Hz by a mechanical chopper (MC2000B-EC, Thorlabs). The other beam is focused onto a sapphire plate to generate a supercontinuum white-light probe. The probe light is dispersed by a monochromator (Omni-λ200i, Zolix) and detected by a CCD (Pascher Instruments). The time delay between pump and probe pulses is controlled by a mechanical delay line. All samples were measured in an optical chamber under a nitrogen atmosphere.

Data Availability

The data supporting the findings of this study are available within the published article and Supplementary Information. The X-ray crystallographic coordinates for structures reported in this study have been deposited at the Cambridge Crystallographic Data Centre (CCDC), under deposition numbers 2522480 (3T) and 2522481 (3T-Cl). These data can be obtained free of charge from the Cambridge Crystallographic Data Centre via www.ccdc.cam.ac.uk/data_request/cif. Source data are provided with this paper.

References

1. Song W, Ye Q, Chen Z, Ge J, Xie L, Ge Z. Advances in stretchable organic photovoltaics: flexible transparent electrodes and deformable active layer design. *Adv Mater* **36**, 2311170 (2024).
2. Zhang Y, Xia H, Yu J, Yang Y, Li G. Materials and device engineering perspective: recent advances in organic photovoltaics. *Adv Mater* **37**, 2504063 (2025).
3. Yan Y, Duan B, Ru M, Gu Q, Li S, Zhao W. Toward flexible and stretchable organic solar cells: a comprehensive review of transparent conductive electrodes, photoactive materials, and device performance. *Adv Energy Mater* **15**, 2404233 (2025).
4. Ma R, *et al.* Organic solar cells: beyond 20%. *Sci China Mater* **68**, 1689-1701 (2025).
5. Lin Y, *et al.* An electron acceptor challenging fullerenes for efficient polymer solar cells. *Adv Mater* **27**, 1170-1174 (2015).
6. Zhao W, *et al.* Molecular optimization enables over 13% efficiency in organic solar cells. *J Am Chem Soc* **139**, 7148-7151 (2017).
7. Yuan J, *et al.* Single-junction organic solar cell with over 15% efficiency using fused-ring acceptor with electron-deficient core. *Joule* **3**, 1140-1151 (2019).
8. Hong L, *et al.* Eco-compatible solvent-processed organic photovoltaic cells with over 16% efficiency. *Adv Mater* **31**, 1903441 (2019).
9. Cui Y, *et al.* Single-junction organic photovoltaic cells with approaching 18% efficiency. *Adv Mater* **32**, 1908205 (2020).
10. Li C, *et al.* Non-fullerene acceptors with branched side chains and improved molecular packing to exceed 18% efficiency in organic solar cells. *Nat Energy* **6**, 605-613 (2021).
11. Cai Y, *et al.* A well-mixed phase formed by two compatible non-fullerene acceptors enables ternary organic solar cells with efficiency over 18.6%. *Adv Mater* **33**, 2101733 (2021).
12. Zhang M, Guo X, Ma W, Ade H, Hou J. A large-bandgap conjugated polymer for versatile photovoltaic applications with high performance. *Adv Mater* **27**, 4655-4660 (2015).
13. Liu Q, *et al.* 18% Efficiency organic solar cells. *Sci Bull* **65**, 272-275 (2020).
14. Cui Y, *et al.* Single-junction organic photovoltaic cell with 19% efficiency. *Adv Mater* **33**, 2102420 (2021).

15. Cai Y, Huo L, Sun Y. Recent advances in wide-bandgap photovoltaic polymers. *Adv Mater* **29**, 1605437 (2017).

16. Fu H, Wang Z, Sun Y. Polymer donors for high-performance non-fullerene organic solar cells. *Angew Chem Int Ed* **58**, 4442-4453 (2019).

17. Zheng Z, Yao H, Ye L, Xu Y, Zhang S, Hou J. PBDB-T and its derivatives: A family of polymer donors enables over 17% efficiency in organic photovoltaics. *Mater Today* **35**, 115-130 (2020).

18. An C, Zheng Z, Hou J. Recent progress in wide bandgap conjugated polymer donors for high-performance nonfullerene organic photovoltaics. *Chem Commun* **56**, 4750-4760 (2020).

19. Liu Y, *et al.* Aggregation and morphology control enables multiple cases of high-efficiency polymer solar cells. *Nat Commun* **5**, 5293 (2014).

20. Zhao J, *et al.* Efficient organic solar cells processed from hydrocarbon solvents. *Nat Energy* **1**, 15027 (2016).

21. Jin Y, *et al.* Thick film polymer solar cells based on naphtho[1,2-c:5,6-c]bis[1,2,5]thiadiazole conjugated polymers with efficiency over 11%. *Adv Energy Mater* **7**, 1700944 (2017).

22. Jiang H, *et al.* A highly crystalline wide-band-gap conjugated polymer toward high-performance as-cast nonfullerene polymer solar cells. *ACS Appl Mater Interfaces* **9**, 36061-36069 (2017).

23. Yuan X, *et al.* Polythiophenes for organic solar cells with efficiency surpassing 17%. *Joule* **6**, 647-661 (2022).

24. Yuan X, *et al.* Achieving 16% efficiency for polythiophene organic solar cells with a cyano-substituted polythiophene. *Adv Funct Mater* **32**, 2201142 (2022).

25. Cha H, *et al.* Exciton and charge carrier dynamics in highly crystalline PTQ10:IDIC organic solar cells. *Adv Energy Mater* **10**, 2070158 (2020).

26. Gao M, *et al.* Tuning the solution aggregation and molecular order for efficient and thermally stable polymer solar cells. *Energy Environ Sci* **16**, 5822-5831 (2023).

27. Wu Z, Wang W, Qian H, Liang Z. Rationalizing star-shaped nonfullerene acceptors in ternary organic solar cells: morphology mediation facilitates exciton and carrier dynamics. *Adv Funct Mater* **35**, 2506436 (2025).

28. Xin J, *et al.* Recent advances in polymorphism of organic solar cells. *Small* **21**, 2409411 (2025).

29. Zhang W, Zhang K, Hao X. Multilength-scale morphological engineering for stable organic solar cells. *Small* **21**, 2412230 (2025).

30. Karki A, *et al.* Unifying charge generation, recombination, and extraction in low-offset non-fullerene acceptor organic solar cells. *Adv Energy Mater* **10**, 2001203 (2020).

31. Gao M, Wang W, Hou J, Ye L. Control of aggregated structure of photovoltaic polymers for high-efficiency solar cells. *Aggregate* **2**, e46 (2021).

32. Yao Z-F, Wang J-Y, Pei J. Controlling morphology and microstructure of conjugated polymers via solution-state aggregation. *Prog Polym Sci* **136**, 101626 (2023).

33. Zheng Y-Q, *et al.* Unraveling the solution-state supramolecular structures of donor–acceptor polymers and their influence on solid-state morphology and charge-transport properties. *Adv Mater* **29**, 1701072 (2017).

34. Li J, *et al.* Nucleation driving force-controlled fibril network formation using a non-halogenated solvent enables polythiophene solar cells with over 18% efficiency. *Energy Environ Sci* **18**, 4384-4395 (2025).

35. Yang N, Zhang S, Cui Y, Wang J, Cheng S, Hou J. Molecular design for low-cost organic photovoltaic materials. *Nat Rev Mater* **10**, 404-424 (2025).

36. Yao H, *et al.* A facile method to fine-tune polymer aggregation properties and blend morphology of polymer solar cells using donor polymers with randomly distributed alkyl chains. *Adv Energy Mater* **8**, 1701895 (2018).

37. Wu Y, *et al.* Fine-tuning semiconducting polymer self-aggregation and crystallinity enables optimal morphology and high-performance printed all-polymer solar cells. *J Am Chem Soc* **142**, 392-406 (2020).

38. Zhang Q, Kelly MA, Bauer N, You W. The curious case of fluorination of conjugated polymers for solar cells. *Acc Chem Res* **50**, 2401-2409 (2017).

39. Li G, Al-Hashimi M, Facchetti A, Marks TJ. Decoding the halogenation cost-performance paradox in organic solar cells. *Nat Rev Mater* **10**, 617-631 (2025).

40. Chao P, Johner N, Zhong X, Meng H, He F. Chlorination strategy on polymer donors toward efficient solar conversions. *J Energy Chem* **39**, 208-216 (2019).

41. Zhao Q, Qu J, He F. Chlorination: an effective strategy for high-performance organic solar cells. *Adv Sci* **7**, 2000509 (2020).

42. Chao P, *et al.* Multichloro-substitution strategy: facing low photon energy loss in nonfullerene solar cells. *ACS Appl Energy Mater* **1**, 6549-6559 (2018).

43. Zhang S, Qin Y, Zhu J, Hou J. Over 14% efficiency in polymer solar cells enabled by a chlorinated polymer donor. *Adv Mater* **30**, 1800868 (2018).

44. Yin B, *et al.* The renaissance of oligothiophene-based donor–acceptor polymers in organic solar cells. *Adv Energy Mater* **12**, 2104050 (2022).

45. Yin B, *et al.* A structurally simple linear conjugated polymer toward practical application of organic solar cells. *Energy Environ Sci* **15**, 4789-4797 (2022).

46. Clark J, Silva C, Friend RH, Spano FC. Role of Intermolecular Coupling in the Photophysics of Disordered Organic Semiconductors: Aggregate Emission in Regioregular Polythiophene. *Phys Rev Lett* **98**, 206406 (2007).

47. Spano FC. The spectral signatures of frenkel polarons in H- and J-aggregates. *Acc Chem Res* **43**, 429-439 (2010).

48. Wang R, *et al.* Understanding the microstructure formation of polymer films by spontaneous solution spreading coating with a high-throughput engineering platform. *ChemSusChem* **14**, 3590-3598 (2021).

49. Clark J, Chang J-F, Spano FC, Friend RH, Silva C. Determining exciton bandwidth and film microstructure in polythiophene films using linear absorption spectroscopy. *Appl Phys Lett* **94**, 163306 (2009).

50. Paquin F, *et al.* Two-dimensional spatial coherence of excitons in semicrystalline polymeric semiconductors: Effect of molecular weight. *Phys Rev B* **88**, 155202 (2013).

51. Dimitriev OP, Blank DA, Ganser C, Teichert C. Effect of the polymer chain arrangement on exciton and polaron dynamics in P3HT and P3HT:PCBM films. *J Phys Chem C* **122**, 17096-17109 (2018).

52. Lu T, Chen F. Multiwfn: A multifunctional wavefunction analyzer. *J Comput Chem* **33**, 580-592 (2012).

53. Bondi A. van der Waals Volumes and Radii. *J Phys Chem* **68**, 441-451 (1964).

54. Politzer P, Murray JS. The use and misuse of van der Waals radii. *Struct Chem* **32**, 623-629 (2021).

55. Liu M, Han X, Chen H, Peng Q, Huang H. A molecular descriptor of intramolecular noncovalent interaction for regulating optoelectronic properties of organic semiconductors. *Nat Commun* **14**, 2500 (2023).

56. Cao Z, *et al.* Variable-temperature scattering and spectroscopy characterizations for temperature-dependent solution assembly of PffBT4T-based conjugated polymers. *ACS Appl Polym Mater* **4**, 3023-3033 (2022).

57. Hammouda B. A new Guinier-Porod model. *J Appl Cryst* **43**, 716-719 (2010).

58. Rivnay J, Mannsfeld SCB, Miller CE, Salleo A, Toney MF. Quantitative determination of organic semiconductor microstructure from the molecular to device scale. *Chem Rev* **112**, 5488-5519 (2012).

59. Müller-Buschbaum P. The active layer morphology of organic solar cells probed with grazing incidence scattering techniques. *Adv Mater* **26**, 7692-7709 (2014).

60. Osaka I, Saito M, Mori H, Koganezawa T, Takimiya K. Drastic change of molecular orientation in a thiazolothiazole copolymer by molecular-weight control and blending with PC61BM leads to high efficiencies in solar cells. *Adv Mater* **24**, 425-430 (2012).

61. Osaka I, Saito M, Koganezawa T, Takimiya K. Thiophene–thiazolothiazole copolymers: significant impact of side chain composition on backbone orientation and solar cell performances. *Adv Mater* **26**, 331-338 (2014).

62. Li M, *et al.* Controlling the surface organization of conjugated donor–acceptor polymers by their aggregation in solution. *Adv Mater* **28**, 9430-9438 (2016).

63. Saito M, Koganezawa T, Osaka I. Understanding comparable charge transport between edge-on and face-on polymers in a thiazolothiazole polymer system. *ACS Appl Polym Mater* **1**, 1257-1262 (2019).

64. Fitri A, *et al.* New materials based on thiazolothiazole and thiophene candidates for optoelectronic device applications: theoretical investigations. *Res Chem Intermed* **39**, 2679-2695 (2013).

65. Jiang Y, *et al.* 20.6% efficiency organic solar cells enabled by incorporating a lower bandgap guest nonfullerene acceptor without open-circuit voltage loss. *Adv Mater* **37**, 2500282 (2025).

66. Wei X, *et al.* Recent progress and applications of nano IR-AFM in morphological characterization of organic solar cells. *Adv Funct Mater* **34**, 2408960 (2024).

67. Ye L, *et al.* Quantitative relations between interaction parameter, miscibility and function in organic solar cells. *Nat Mater* **17**, 253-260 (2018).

68. Bi Z, Liu C, Ma W. In situ morphology control for solution-printable organic photovoltaics. *Adv Funct Mater* **34**, 2409315 (2024).

69. Ren J, *et al.* Manipulating aggregation kinetics toward efficient all-printed organic solar cells. *Adv Mater* **37**, 2418353 (2025).

70. Blom PWM, Mihailetchi VD, Koster LJA, Markov DE. Device physics of polymer:fullerene bulk heterojunction solar cells. *Adv Mater* **19**, 1551-1566 (2007).

71. Koster LJA, Mihailetchi VD, Ramaker R, Blom PWM. Light intensity dependence of open-circuit voltage of polymer:fullerene solar cells. *Appl Phys Lett* **86**, 123509 (2005).

72. Mandoc MM, Kooistra FB, Hummelen JC, de Boer B, Blom PWM. Effect of traps on the performance of bulk heterojunction organic solar cells. *Appl Phys Lett* **91**, 263505 (2007).

73. Kyaw AKK, *et al.* Intensity dependence of current–voltage characteristics and recombination in high-efficiency solution-processed small-molecule solar cells. *ACS Nano* **7**, 4569-4577 (2013).

74. Cowan SR, Street RA, Cho S, Heeger AJ. Transient photoconductivity in polymer bulk heterojunction solar cells: Competition between sweep-out and recombination. *Phys Rev B* **83**, 035205 (2011).

75. Kirchartz T, *et al.* Sensitivity of the Mott–Schottky analysis in organic solar cells. *J Phys Chem C* **116**, 7672-7680 (2012).

76. Scaccabarozzi AD, *et al.* Doping approaches for organic semiconductors. *Chem Rev* **122**, 4420-4492 (2022).

77. Haneef HF, Zeidell AM, Jurchescu OD. Charge carrier traps in organic semiconductors: a review on the underlying physics and impact on electronic devices. *J Mater Chem C* **8**, 759-787 (2020).

78. Yao W, *et al.* Organic bulk heterojunction infrared photodiodes for imaging out to 1300 nm. *ACS Appl Electron Mater* **1**, 660-666 (2019).

Acknowledgements

The research was supported by National Natural Science Foundation of China: 22275058 (C.D.), 22405092 (B.W.), 52403225 (X.Y.), National Key Research and Development Program of China: 2024YFB4611500 (C.D.), Guangdong Provincial Science and Technology Plan Project: 2023A0505010003 (C.D.), Guangdong Basic and Applied Basic Research Foundation: 2022B1515120008 (C.D.), 2025A1515010221 (B.W.), and Guangdong Innovative and Entrepreneurial Research Team Program: 2019ZT08L075 (C.D.), and China Postdoctoral Science Foundation: GZC20250122 (B.Y.), 2025M770181 (B.Y.), 2023TQ0120 (X.Y.), GZB20230223 (X.Y.). We also gratefully acknowledge the staff members of the Very Small Angle Neutron Scattering and Small Angle Neutron Scattering at the China Spallation Neutron Source (CSNS), especially Dr. Qing Chen and Dr. Zhenhua Xie for providing technical support, and thank Prof. Long Ye and Saimeng Li from Tianjin University for their assistance with GIWAXS analysis.

Author Contributions

C. D. conceived the idea and supervised the project. B. Y. performed device fabrication and data analysis. Z. C. and B. W. synthesized the polymers. X. Y. performed the synthesis complexity analysis. C. X. and X. Z. contributed to the single crystal structure analysis. J. Z. and W. Z. performed the transient absorption measurements and data analysis. S. L. and C. Y. performed the GIWAXS analysis. W. C. and G. Z. did the energy loss measurement. L. Z. did the in-situ absorption measurement. L. W. performed the SANS measurement and analysis. Z. L., F. H., and Y. C. participated in project administration. B. Y., Z. C., B. W. and C. D. prepared the manuscript. All authors commented on the manuscript.

Competing Interests

The authors declare no competing interests.

Table 1. Device parameters of the OSCs based on PTTz-Cl*x*:BTP-eC9 blends under AM1.5G (100 mW cm^{-2}) irradiation.

Device	V_{oc} (V)	J_{sc} (mA cm^{-2})	$J_{cal.}$ (mA cm^{-2})	FF (%)	PCE (%)
PTTz-Cl0:BTP-eC9	0.826 (0.824±0.002)	27.27 (27.40±0.15)	26.18	76.83 (75.51±0.98)	17.30 (17.05±0.18)
PTTz-Cl50:BTP-eC9	0.856 (0.853±0.002)	29.79 (29.41±0.32)	28.25	80.13 (79.10±0.62)	20.42 (19.85±0.33)
PTTz-Cl100:BTP-eC9	0.866 (0.864±0.002)	25.95 (25.36±0.81)	24.61	69.72 (69.37±1.64)	15.67 (15.18±0.26)

Fig. 1. Molecular design and aggregation behavior. a Chemical structure of the PTTz-Cl*x* polymers. **b** Crystal structures of the model compounds 3T and 3T-Cl. **c** Temperature-dependent absorption spectra of the polymers in chlorobenzene solutions. **d** Relative aggregation strength of the polymers at different temperatures. **e** SANS curves of the polymers in $CDCl_3$ solution. Source data are provided as a Source Data file.

Fig. 2. Molecular packing in neat polymer films. a 2D GIWAXS patterns. **b** 1D line-cut profiles in OOP and IP direction. **c** Azimuthal integration (pole figures) of the (010) π-π stacking peak. **d** Quantified face-on and edge-on orientation populations. Source data are provided as a Source Data file.

Fig. 3. Morphology of the blend films. a-c TEM images. Scale bar: 200 nm. **d-f** AFM height images. Scale bar: 400 nm. **g–i** AFM-IR chemical distribution maps.

Fig. 4. Film formation kinetics of the blends. a-c Time-dependent UV–vis absorption spectra during solvent drying. **d-f** Evolution of the peak position and intensity for the donor and acceptor. **g** Schematic diagram of the phase evolution leading to optimal morphology. Reprinted from Current Opinion in Green and Sustainable Chemistry, 5, Caitlin McDowell, Guillermo C. Bazan, Organic solar cells processed from green solvents, 49-54, Copyright (2017), with permission from Elsevier. Source data are provided as a Source Data file.

Fig. 5. Photovoltaic performance and device physics. a *J*–*V* curves of the optimal devices. **b** EQE spectra. **c** Statistical distribution of PCEs for devices based on linear conjugated polymer donors. **d** Electron and hole mobilities extracted from single-carrier devices. **e** V_{oc} versus light intensity. **f** TPV decay kinetics. **g** TPC decay kinetics. **h** Mott-Shockley plots. **i** DOS distribution derived from C–*f* measurements. Source data are provided as a Source Data file.

Fig. 6. Transient absorption spectroscopy analysis. a-c TA color maps of the blend films after 800 nm excitation. **d-f** TA spectra obtained from panels . **g-i** TA kinetics probed at the acceptor (820 nm) and donor (610 nm) ground-state bleach signals. Source data are provided as a Source Data file.

Editor's Summary

Yin et al. report linear conjugated polymer donors with chlorinated backbone for modulating polymer aggregation and surface tension, and optimised compatibility with norfullerene acceptors. By using binary blends, a 20.42% efficiency is achieved for organic solar cells.

Peer review information: *Nature Communications* thanks the anonymous reviewer(s) for their contribution to the peer review of this work. A peer review file is available.

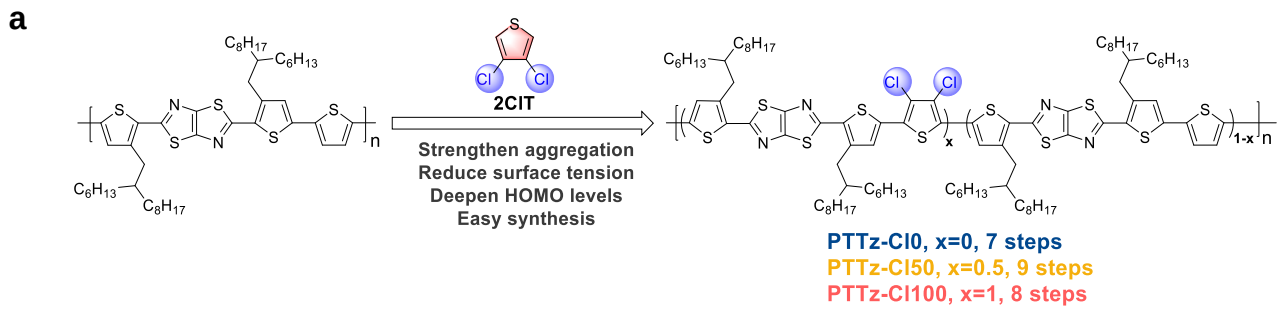
a
2CIT
Strengthen aggregation
Reduce surface tension
Deepen HOMO levels
Easy synthesis
PTTz-Cl0, x=0, 7 steps
PTTz-Cl50, x=0.5, 9 steps
PTTz-Cl100, x=1, 8 steps

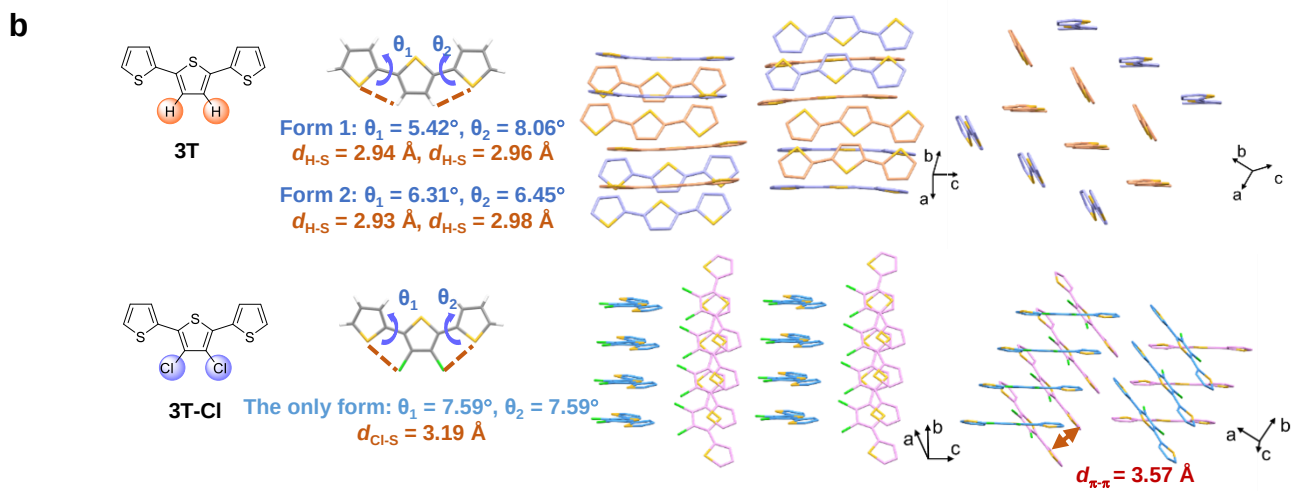
b
3T
Form 1: θ1 = 5.42°, θ2 = 8.06°
dH-S = 2.94 Å, dH-S = 2.96 Å
Form 2: θ1 = 6.31°, θ2 = 6.45°
dH-S = 2.93 Å, dH-S = 2.98 Å
3T-Cl
The only form: θ1 = 7.59°, θ2 = 7.59°
dCl-S = 3.19 Å
dπ-π = 3.57 Å

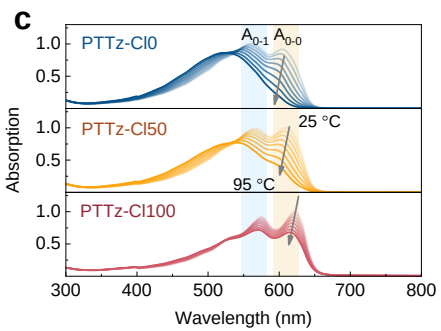
c
PTTz-Cl0
PTTz-Cl50
PTTz-Cl100
A0-1
A0-0
25 °C
95 °C
Absorption
Wavelength (nm)

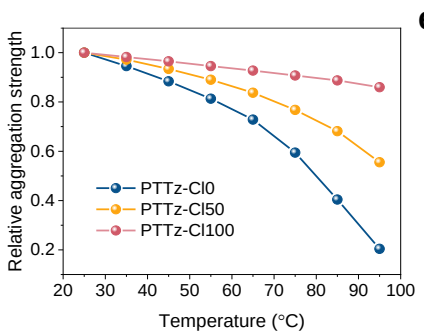
d
Relative aggregation strength
Temperature (°C)
PTTz-Cl0
PTTz-Cl50
PTTz-Cl100

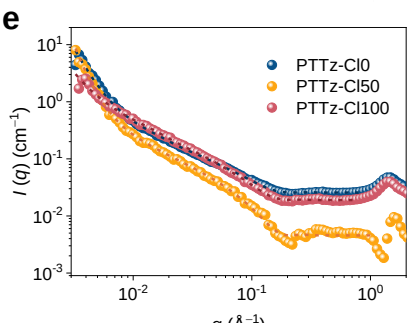
e
I (q) (cm−1)
q (Å−1)
PTTz-Cl0
PTTz-Cl50
PTTz-Cl100

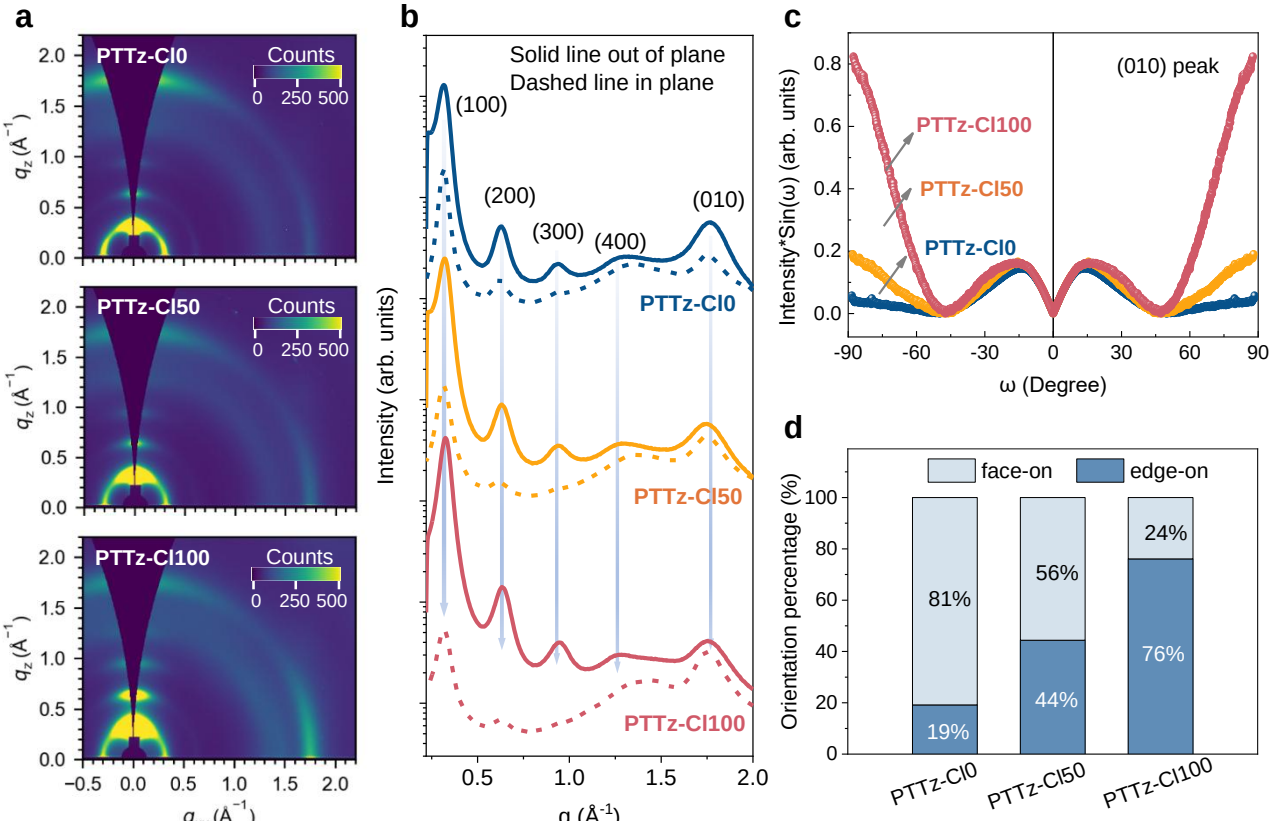
a
PTTz-Cl0
Counts
0 250 500
PTTz-Cl50
PTTz-Cl100
q_z (Å^{-1})
q_{xy} (Å^{-1})
b
Solid line out of plane
Dashed line in plane
(100)
(200)
(300)
(400)
(010)
PTTz-Cl0
PTTz-Cl50
PTTz-Cl100
Intensity (arb. units)
q (Å^{-1})
c
(010) peak
PTTz-Cl100
PTTz-Cl50
PTTz-Cl0
Intensity*Sin(ω) (arb. units)
ω (Degree)
d
face-on
edge-on
Orientation percentage (%)
81%
19%
56%
44%
24%
76%
PTTz-Cl0
PTTz-Cl50
PTTz-Cl100

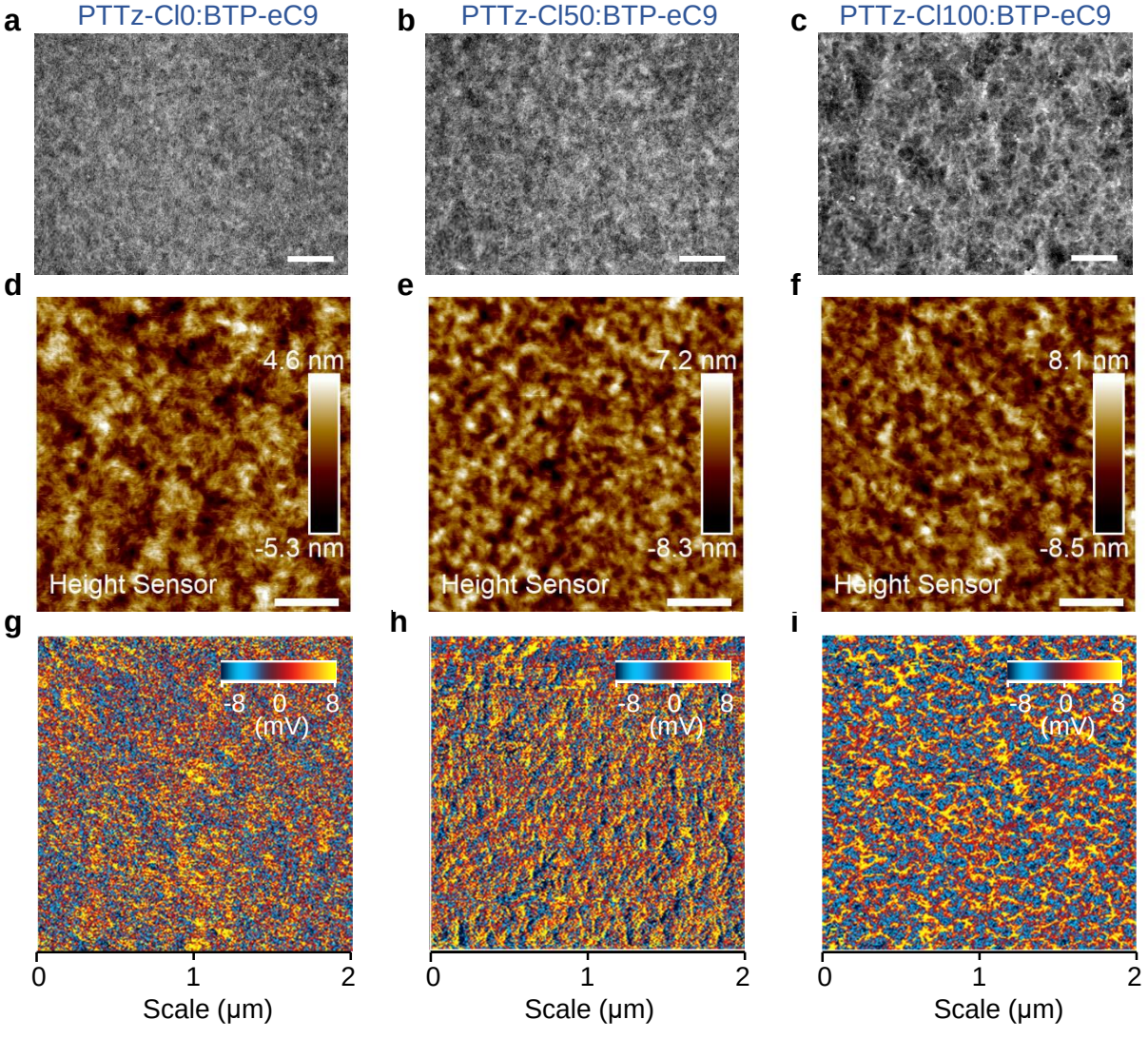
a
PTTz-Cl0:BTP-eC9
b
PTTz-Cl50:BTP-eC9
c
PTTz-Cl100:BTP-eC9
d
4.6 nm
-5.3 nm
Height Sensor
e
7.2 nm
-8.3 nm
Height Sensor
f
8.1 nm
-8.5 nm
Height Sensor
g
-8 0 8
(mV)
h
-8 0 8
(mV)
i
-8 0 8
(mV)
0 1 2
Scale (μm)
0 1 2
Scale (μm)
0 1 2
Scale (μm)

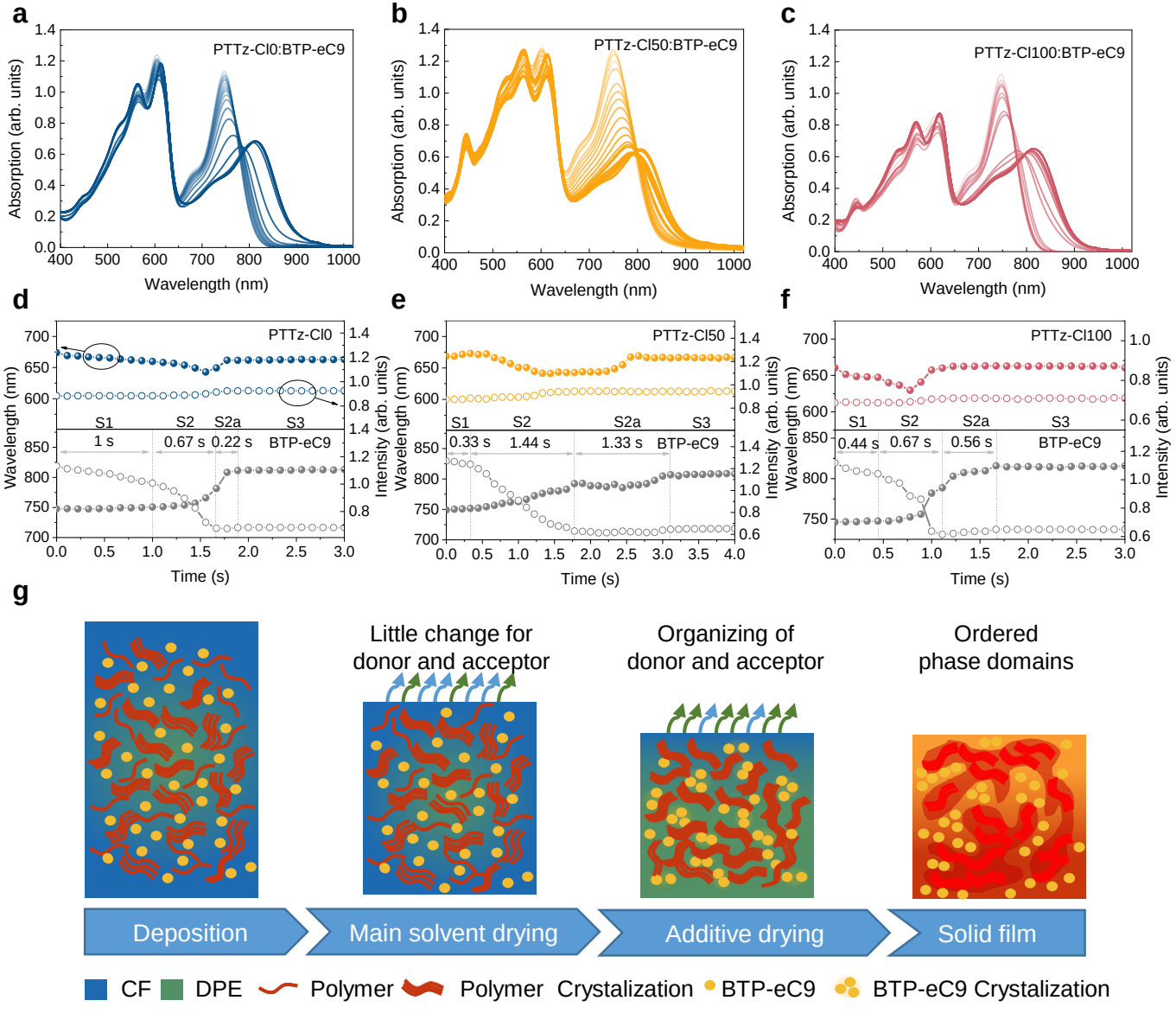
a
PTTz-Cl0:BTP-eC9
Absorption (arb. units)
Wavelength (nm)
b
PTTz-Cl50:BTP-eC9
Absorption (arb. units)
Wavelength (nm)
c
PTTz-Cl100:BTP-eC9
Absorption (arb. units)
Wavelength (nm)
d
PTTz-Cl0
S1
S2
S2a
S3
1 s
0.67 s
0.22 s
BTP-eC9
Wavelength (nm)
Intensity (arb. units)
Time (s)
e
PTTz-Cl50
S1
S2
S2a
S3
0.33 s
1.44 s
1.33 s
BTP-eC9
Wavelength (nm)
Intensity (arb. units)
Time (s)
f
PTTz-Cl100
S1
S2
S2a
S3
0.44 s
0.67 s
0.56 s
BTP-eC9
Wavelength (nm)
Intensity (arb. units)
Time (s)
g
Little change for donor and acceptor
Organizing of donor and acceptor
Ordered phase domains
Deposition
Main solvent drying
Additive drying
Solid film
CF
DPE
Polymer
Polymer Crystalization
BTP-eC9
BTP-eC9 Crystalization

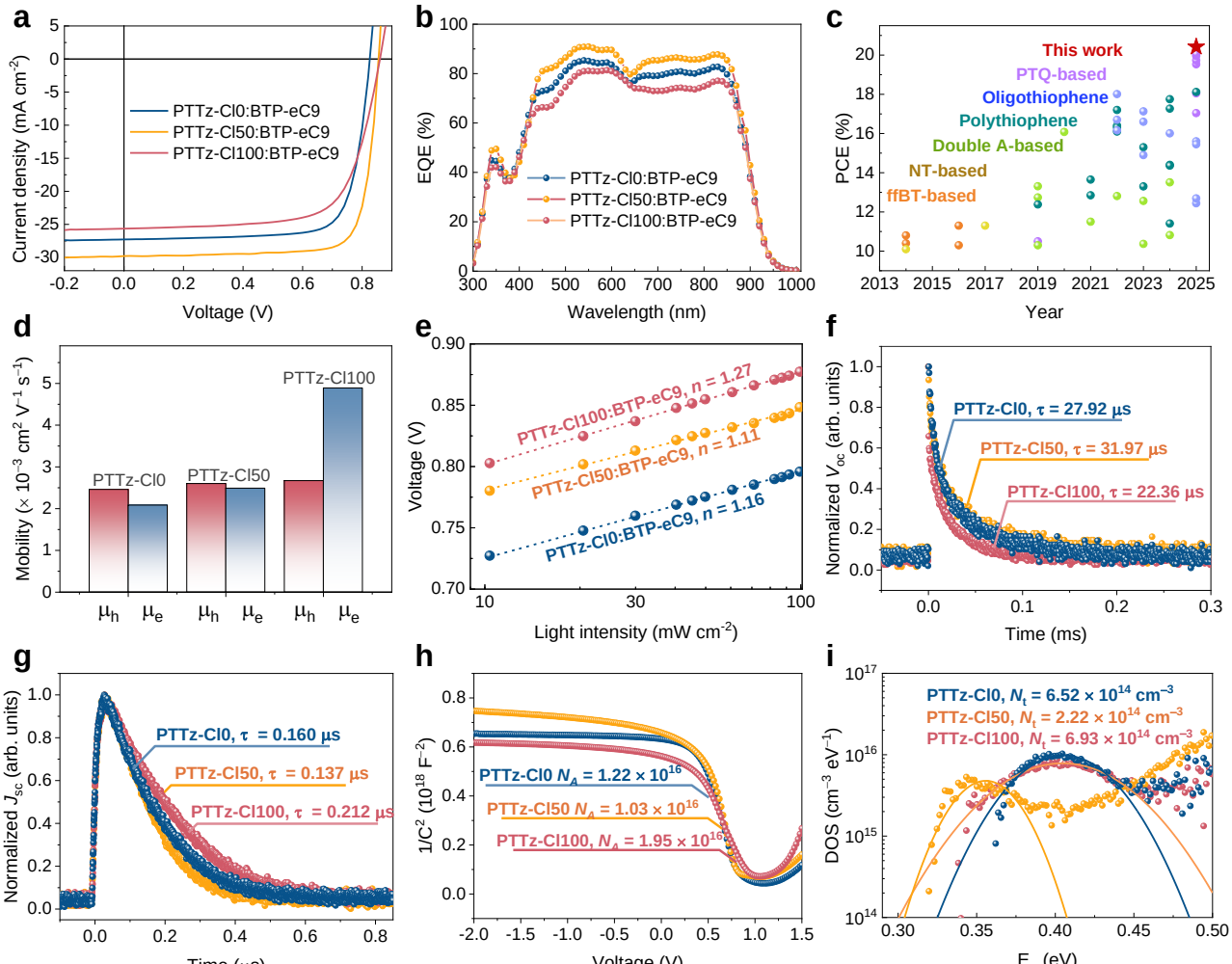
a
Current density (mA cm^{-2})
Voltage (V)
PTTz-Cl0:BTP-eC9
PTTz-Cl50:BTP-eC9
PTTz-Cl100:BTP-eC9
b
EQE (%)
Wavelength (nm)
PTTz-Cl0:BTP-eC9
PTTz-Cl50:BTP-eC9
PTTz-Cl100:BTP-eC9
c
PCE (%)
Year
This work
PTQ-based
Oligothiophene
Polythiophene
Double A-based
NT-based
ffBT-based
d
Mobility (× 10^{-3} cm^2 V^{-1} s^{-1})
PTTz-Cl0
PTTz-Cl50
PTTz-Cl100
μ_h μ_e μ_h μ_e μ_h μ_e
e
Voltage (V)
Light intensity (mW cm^{-2})
PTTz-Cl100:BTP-eC9, n = 1.27
PTTz-Cl50:BTP-eC9, n = 1.11
PTTz-Cl0:BTP-eC9, n = 1.16
f
Normalized V_{oc} (arb. units)
Time (ms)
PTTz-Cl0, τ = 27.92 μs
PTTz-Cl50, τ = 31.97 μs
PTTz-Cl100, τ = 22.36 μs
g
Normalized J_{sc} (arb. units)
Time (μs)
PTTz-Cl0, τ = 0.160 μs
PTTz-Cl50, τ = 0.137 μs
PTTz-Cl100, τ = 0.212 μs
h
1/C^2 (10^{18} F^{-2})
Voltage (V)
PTTz-Cl0 N_A = 1.22 × 10^{16}
PTTz-Cl50 N_A = 1.03 × 10^{16}
PTTz-Cl100, N_A = 1.95 × 10^{16}
i
DOS (cm^{-3} eV^{-1})
E_ω (eV)
PTTz-Cl0, N_t = 6.52 × 10^{14} cm^{-3}
PTTz-Cl50, N_t = 2.22 × 10^{14} cm^{-3}
PTTz-Cl100, N_t = 6.93 × 10^{14} cm^{-3}

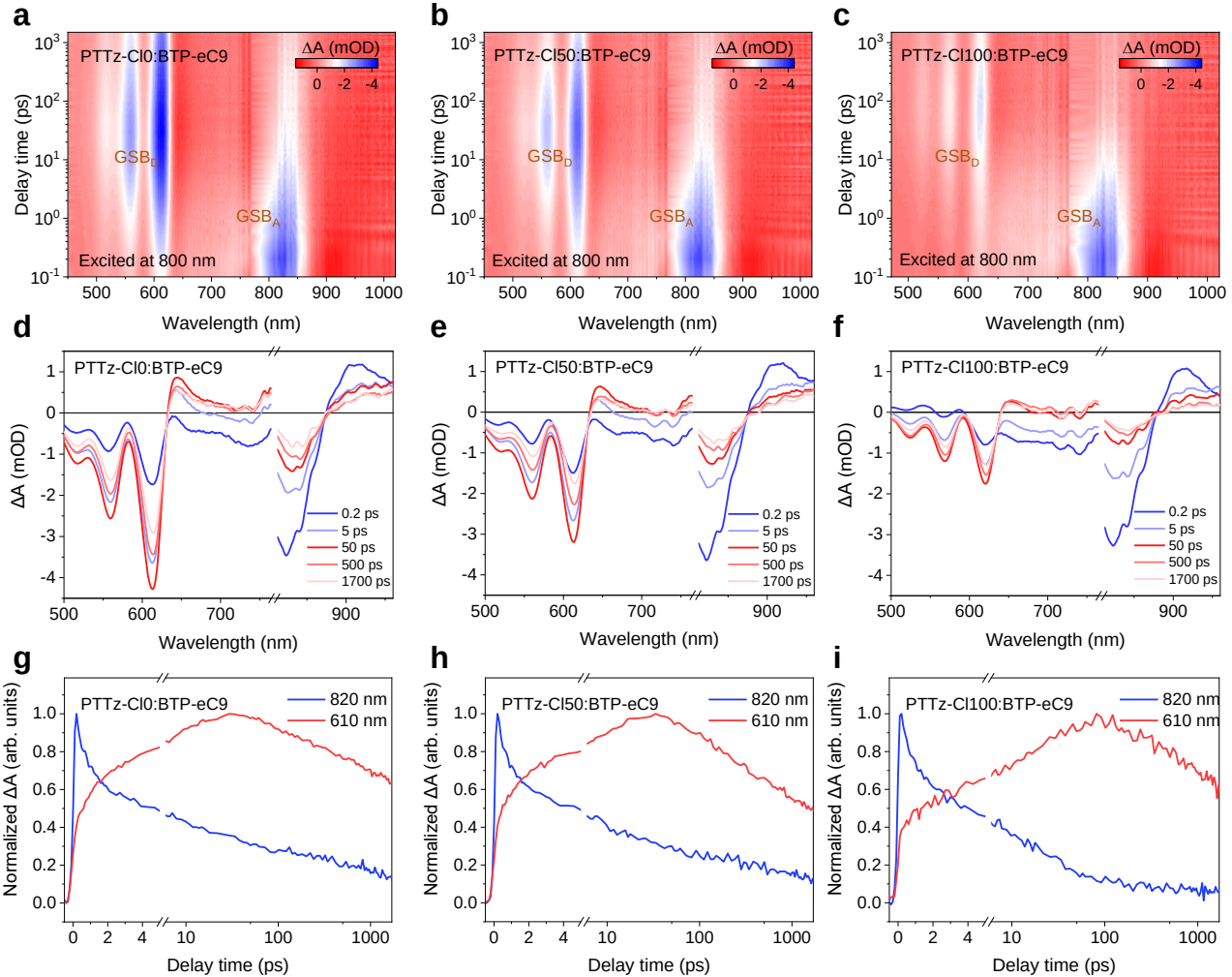
a
PTTz-Cl0:BTP-eC9
ΔA (mOD)
0 -2 -4
GSB$_D$
GSB$_A$
Excited at 800 nm
Delay time (ps)
Wavelength (nm)
b
PTTz-Cl50:BTP-eC9
c
PTTz-Cl100:BTP-eC9
d
PTTz-Cl0:BTP-eC9
ΔA (mOD)
0.2 ps
5 ps
50 ps
500 ps
1700 ps
e
PTTz-Cl50:BTP-eC9
f
PTTz-Cl100:BTP-eC9
g
PTTz-Cl0:BTP-eC9
820 nm
610 nm
Normalized ΔA (arb. units)
h
PTTz-Cl50:BTP-eC9
i
PTTz-Cl100:BTP-eC9